PNAS RESEARCH ARTICLE | BIOPHYSICS AND COMPUTATIONAL BIOLOGY
MICROBIOLOGY

Geometrical control of interface patterning underlies active matter invasion

Haoran Xu[a,b], Mehrana R. Nejad[c], Julia M. Yeomans[c], and Yilin Wu[a,b,1]

Edited by M. Cristina Marchetti, University of California, Santa Barbara, CA; received November 18, 2022; accepted June 16, 2023

Interaction between active materials and the boundaries of geometrical confinement is key to many emergent phenomena in active systems. For living active matter consisting of animal cells or motile bacteria, the confinement boundary is often a deformable interface, and it has been unclear how activity-induced interface dynamics might lead to morphogenesis and pattern formation. Here, we studied the evolution of bacterial active matter confined by a deformable boundary. We found that an ordered morphological pattern emerged at the interface characterized by periodically spaced interfacial protrusions; behind the interfacial protrusions, bacterial swimmers self-organized into multicellular clusters displaying +1/2 nematic defects. Subsequently, a hierarchical sequence of transitions from interfacial protrusions to creeping branches allowed the bacterial active drop to rapidly invade surrounding space with a striking self-similar branch pattern. We found that this interface patterning is geometrically controlled by the local curvature of the interface, a phenomenon we denote as collective curvature sensing. Using a continuum active model, we revealed that the collective curvature sensing arises from enhanced active stresses near high-curvature regions, with the active length scale setting the characteristic distance between the interfacial protrusions. Our findings reveal a protrusion-to-branch transition as a unique mode of active matter invasion and suggest a strategy to engineer pattern formation of active materials.

biological active matter | interface growth | pattern formation | self-organization | bacterial swarming

As a prototype of active matter (1), active fluids consist of force-generating units suspended in a liquid medium (2), such as suspensions of motile bacteria (3–5), animal tissues (6, 7), and cytoskeleton components driven by molecular motors (8, 9). Interaction between active fluids and the boundaries of geometrical confinement has been shown to support rich emergent phenomena, such as cell sorting (10, 11), spontaneous flow (9, 12), vortex formation (13, 14), and ordering (15). These emergent phenomena are primarily observed in active fluids interacting with hard confining walls. However, for living active fluids in natural environments or in clinical settings, the confinement boundary is often a soft and deformable interface. For example, the collective invasion of mesenchymal cancer cells pushes against soft tissue layers (16, 17); surface-associated bacterial communities (or biofilms) can grow as droplets on solid substrates where the interfacial mechanics is key to their development (18, 19). Activity-induced boundary deformation or interface growth enables active matter invasion into the surrounding space (20–23), and it is a key process that governs the morphogenesis and pattern formation of active materials (24–29).

Motile bacteria are premier model systems for active matter (1, 2). Here, we studied the evolution of bacterial active fluids confined by a deformable boundary, i.e., the three-phase (air–liquid–solid) interface. Our experimental setup consists of drops of suspended motile bacteria grown on solid substrates; this configuration resembles the initial stages of growing bacterial colonies and biofilms commonly found in the natural environment and during pathogenesis (18). We found that an ordered morphological pattern emerged at the interface, characterized by periodically spaced interfacial protrusions. Behind the interfacial protrusions, bacterial swimmers self-organized into multicellular clusters each displaying a +1/2 nematic defect, and the collective velocity field of cells adjacent to the invasion interface was organized into a 1D vortex lattice. Some of the interfacial protrusions eventually broke out as creeping branches, and the branches continued to experience the protrusion-to-branch transition in a hierarchical manner, allowing the bacterial active fluid to rapidly invade the surrounding space with a striking self-similar branch pattern. We found that the interface patterning of active suspension drops is controlled by interface geometry via a mechanism we denote as collective curvature sensing: Both the interfacial protrusion amplitude and the probability of the protrusion-to-branch transition are positively correlated with the local curvature of the drop boundary. We developed a continuum active matter model that reproduces the interface morphology and revealed that the

Significance

Biological active matter consisting of living cells often invades the surrounding space via activity-induced boundary deformation or interface growth. Examples include tumor invasion and bacterial colony expansion. Here, we describe a unique mode of invasion and pattern formation in bacterial active matter. In this mode, active drops of bacterial suspensions develop regularly spaced interfacial protrusions at the edge; the protrusions further transform into creeping branches in a hierarchical, self-similar manner, with the transition probability depending on the interface geometry (i.e., local curvature). Our findings show that interface geometry may play important roles in active matter morphogenesis and suggest a strategy to manipulate pattern formation in active materials.

Author affiliations: [a]Department of Physics, The Chinese University of Hong Kong, Shatin, NT, Hong Kong, People's Republic of China; [b]Shenzhen Research Institute, The Chinese University of Hong Kong, Shatin, NT, Hong Kong, People's Republic of China; and [c]Department of Physics, The Rudolf Peierls Centre for Theoretical Physics, University of Oxford, Oxford OX1 3PU, United Kingdom

---

Author contributions: H.X. and Y.W. designed the experiments and M.R.N. and J.M.Y. designed the simulations; H.X. performed the experiments and M.R.N. performed and interpreted the simulations; Y.W. contributed new reagents/analytic tools; H.X. and Y.W. analyzed data; and H.X., M.R.N., J.M.Y., and Y.W. wrote the paper.

The authors declare no competing interest.

This article is a PNAS Direct Submission.

[1]To whom correspondence may be addressed. Email: ylwu@cuhk.edu.hk.

This article contains supporting information online at https://www.pnas.org/lookup/suppl/doi:10.1073/pnas.2219708120/-/DCSupplemental.

collective curvature sensing arises from enhanced active forces near high-curvature regions. Our findings illustrate the key role of interface geometry in active matter invasion and pattern formation. The protrusion-to-branch transition as a unique mode of space exploration is also relevant to the expansion and dispersal of bacterial communities in natural environments (18).

Results

Ordered Protrusions and Self-Organization at an Active Fluid Interface. We used quasi-2D circular drops containing a suspension of *Proteus mirabilis* grown on an agar substrate as a model active fluid (*Methods*). *P. mirabilis* is a gram-negative, rod-shaped bacterium, widely distributed in the natural environment (30). It is well known for having vigorous flagellar motility on agar surfaces (31). We monitored how the active suspension drops of *P. mirabilis* (~4 µm in length and 0.8 µm in width in our growth conditions) started to spread on solid substrates with low wettability (*Methods*). Initially, the interface between the active drop and the cell-free space was smooth. As time evolved, the interface was gradually deformed, and the active drop developed an ordered morphological pattern at the interface (Fig. 1 *A* and *B*, *Upper* and Movie S1). This was characterized by periodically spaced protrusions along the interface, with an interprotrusion separation of 65 ± 9 µm (mean ± SD) (Fig. 1*C*). Behind the interfacial protrusions, bacterial swimmers self-organized into multicellular clusters, commensurate with the protrusions, with a length (from base to tip) of ~10 to 30 µm. The orientation field of cells in each cluster displayed a +1/2 nematic defect with the polarity vector (32) pointing perpendicular to the interface and toward the colony center (Fig. 1 *B*, *Middle* and Movie S1). Meanwhile, the collective velocity field of cells adjacent to the interface self-organized into a vortex lattice, with neighboring domains of opposite vorticity (Fig. 1 *B*, *Lower*). The vortices were primarily extended perpendicular to the interface, and the domain size was, on average, 1/2 of the interprotrusion separation (Fig. 1 *B*, *Lower*). The vortex lattice was highly stable in time, as shown by the strong temporal correlations (Fig. 1*D*).

To examine whether the interface morphological pattern and bacterial self-organization were driven by bacterial motility, we optically deactivated the flagellar motility of cells at the invasion interface with violet light illumination (14) (*Methods*). During light-induced motility deactivation, the interfacial protrusions gradually smoothed out and cells near the edge became aligned parallel to the interface (*SI Appendix*, Fig. S1 and Movie S2). Meanwhile, all the multicellular clusters as well as the vortex structure of the cellular collective velocity field near the interface disappeared. After withdrawal of light, cell motility recovered, and the interfacial protrusions reemerged (*SI Appendix*, Fig. S1 and Movie S2). As the growth activity of most cells in the active drop was not affected during motility deactivation (note that only cells at the edge were illuminated by light), our result showed that active stress due to flagellar motility is necessary to form the interface morphological pattern and cellular self-organization, while the effect of cell mass growth alone cannot account for the phenomenon (33). On the other hand, bacterial suspension drops consisting of cells that were washed and deposited on fresh substrates developed the same interfacial morphology within ~10 min (*SI Appendix*, Fig. S2 and Movie S3; *Methods*); this fact rules out the contribution of Marangoni instability (34–37), chemotaxis (38), or intercellular chemical signaling (39) to the phenomena.

Hierarchical Transition from Interfacial Protrusions to Creeping Branches. After the emergence of the interfacial pattern, some protrusions of the active suspension drop started to expand continuously at a speed of several µm/s (up to ~10 µm/s) in the form of creeping branches (Fig. 2*A* and Movie S4). The first creeping branches later underwent the same protrusion-to-branch transition process (Fig. 2*A*): Protrusions developed at the interface between the creeping branches and the open space, and some of these protrusions broke out as secondary creeping branches. The secondary creeping branches again repeated this process to give rise to new creeping branches at the next level. The protrusion-to-branch transition continued recursively in a hierarchical manner, with the creeping branches at all levels of hierarchy having a

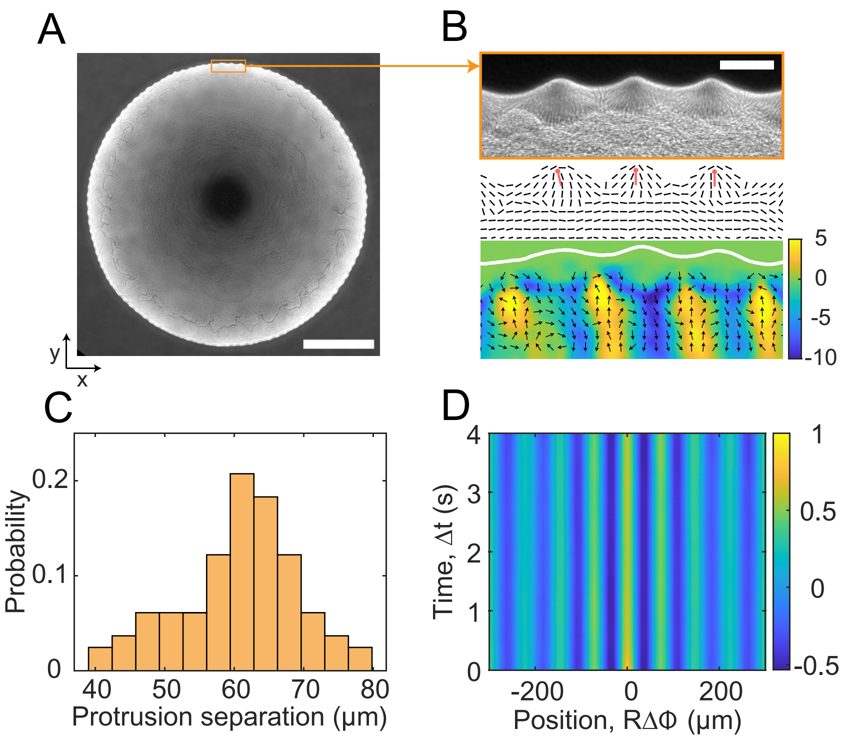

Fig. 1. Ordered interfacial protrusions and bacterial self-organization near an active fluid interface. (*A*) Representative phase-contrast image of a *P. mirabilis* active suspension drop with ordered interfacial protrusions. (Scale bar, 500 µm.) (*B*) *Upper*: Enlarged view of the box in panel *A*. *Middle*: Orientation field of cells in the *Upper* panel computed based on the gradient field of the phase-contrast image (*Methods*). Red marks represent the direction of +1/2 defects, with the dot indicating the defect core. *Lower*: Colormap showing the averaged velocity field at the region shown in the *Upper* panel computed by optical flow analysis on phase-contrast images (*Methods*). The collective velocity field was averaged over a duration of 10 s. Arrows in the figure represent velocity direction while the colormap at the right indicates the radial velocity component (unit: µm/s). A positive value indicates moving outward toward the interface, while a negative value indicates moving inward away from the interface. (Scale bar, 50 µm.) (*C*) Distribution of the nearest separation of interfacial protrusions. (*D*) Spatial–temporal correlation of the radial velocity adjacent to the interface. The definition of spatial-temporal correlation function $C(\Delta\phi, \Delta t) \sim \langle v_r(R,\phi,t)v_r(R,\phi+\Delta\phi,t+\Delta t)\rangle_{\phi,t}$ is provided in *Methods*. On the horizontal axis, R represents the radius of the active suspension drop, and θ is the polar angle.

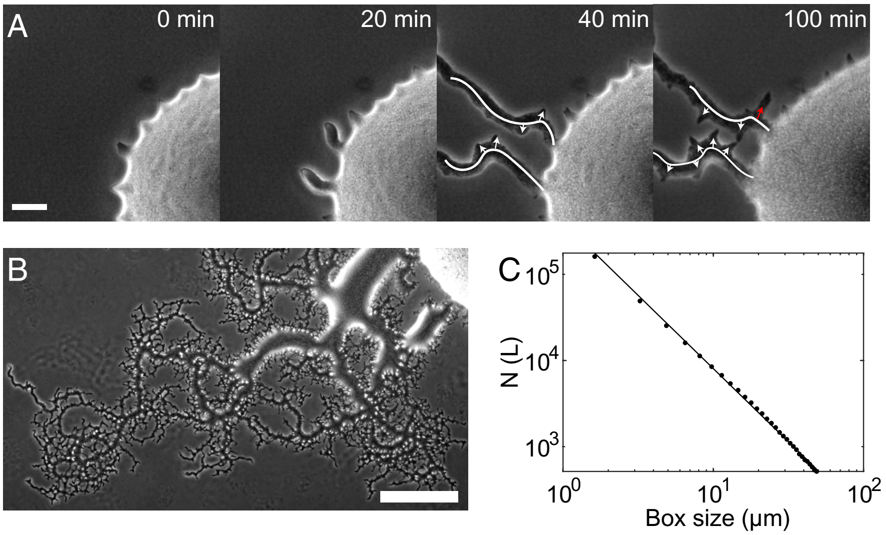

Fig. 2. Hierarchical transition from interfacial protrusions to creeping branches. (*A*) Image sequence showing the transition from interfacial protrusions to creeping branches. (Scale bar, 50 μm.) T = 0 min is chosen at the onset of the protrusion-to-branch transition. White arrows on the T = 40-min and 100-min images represent the protrusions formed on the first branches, and the red arrow at T = 100 min indicates a position where a secondary creeping branch is forming. (*B*) Self-similar pattern resulting from the recursive and hierarchical protrusion-to-branch transition process. The brighter region at the upper-right corner is the edge of the active suspension drop. (Scale bar, 500 μm.) (*C*) Analysis of the fractal-like branch pattern by the box counting method (40–42). To calculate the fractal dimension D_f of creeping branch patterns, an image of creeping branches was first divided into a lattice of square domains of size $L \times L$. The number of squares that covered the pattern of interest (i.e., creeping branches) were counted and denoted as $N(L)$. Repeating this procedure yielded $N(L)$ as a function of box size L plotted here in the log–log scale. The plot is well fitted by a straight line $\log N \sim -D_f \log L$, suggesting that the branch pattern has self-similarity, and $D_f = 1.70$ is taken as the fractal dimension.

conserved initial width of ~20 to 30 μm (Fig. 2*A* and Movies S4 and S5). Interestingly, the width of protrusions [~20 to 30 μm; defined as the full width at half maximum (FWHM) of the protrusion profile] is comparable to the initial branch width and also conserved across all levels of hierarchal creeping branches (Figs. 1*B* and 2*A* and Movies S4 and S5), even on the last-level branches which have a width of ~20 μm (*SI Appendix*, Figs. S3 and S4). This fact suggests that the protrusion width is controlled by some intrinsic length scale, and the characteristic protrusion width sets the initial or the minimal width of creeping branches. We note that once a creeping branch has formed, cell mass growth can help the formation of higher-level branching by supplying more cell mass and by widening the branch widths. Also, two creeping branches colliding with each other would merge into one. Due to branch widening and merging, a general trend is that earlier branches become wider than later ones (Movie S5). Not all protrusions eventually develop into creeping branches; as a protrusion started to expand, we found that the amplitude of nearby protrusions would decrease and even disappear (*SI Appendix*, Fig. S5), suggesting that cells are being drawn to support the expansion of a nearby existing creeping branch.

The recursive and hierarchical transition process gives rise to a striking self-similar pattern (Fig. 2*B* and Movie S5). To characterize this pattern, we computed its fractal dimension D_f and found it to be 1.70 (Fig. 2*C*) (40). The fractal dimension is close to that reported for branching patterns of bacterial colonies (41, 42). However, here, the fractal-like branching pattern of the active suspension drop is driven by defect-mediated active stresses, which is in contrast to the fractal-like branching patterns of bacterial colonies due to reaction–diffusion processes involving the coupling between cell mass growth and nutrient or chemoattractant fields (41, 42). Indeed, cell mass growth alone does not give rise to fractal-like colony morphology in *P. mirabilis* under our experimental conditions since sessile colonies where most cells have become immotile but keep growing only expand in a rounded shape. However, since cell mass growth can widen the stripes, it affects the fractal dimension. Fractal-like branching patterns arising from chemotactic movement of cells are also found in slime molds (43–46). Particularly, the hierarchal narrowing of creeping branches in bacterial active drops is reminiscent of the hierarchal tube diameters in the network growth of slime mold *Physarum* (45, 46). We note that the protrusion-to-branch pattern of active drop invasion is distinct from the fingering pattern of bacterial colonies driven by Marangoni instability in the presence of surface tension gradients (35–37), which requires biosurfactant synthesis and is independent of cell motility.

Interface Curvature Controls Protrusion Amplitude and the Probability of a Protrusion-to-Branch Transition. When working with active suspension drops of an anisotropic shape, we noticed that the first creeping branches were more likely to emanate from higher-curvature regions (Fig. 3*A*). To rationalize this observation, we investigated the behavior of interfacial protrusions in active suspension drops with different shapes. We found that the amplitude of the interfacial protrusions was positively correlated with the baseline curvature of the interface (i.e., the local curvature computed by smoothing out interfacial protrusions) (Fig. 3*B*; *Methods*). For instance, the protrusion amplitude near the poles (of higher curvature) of an elongated drop was significantly greater than elsewhere, while the interprotrusion separation remained the same (Fig. 3*C*). Moreover, examination of the full hierarchical branching pattern of active suspension drops revealed that the probability of a protrusion-to-branch transition increased with the baseline curvature of the interface (Fig. 3*D*; *Methods*). These results show that the bacterial cells respond to mesoscale curvature (on a length scale much larger than single cell size) of the interface of active suspension drops and branches in a collective manner to drive the dynamics of interfacial protrusions. Here, "collective" means that the change in the shape of the interface is caused by the collective interactions of many bacteria, rather than single cells; this is in contrast to curvotaxis of migrating cells where single cells respond to cell-scale curvature variations (47). Therefore, we denote the phenomenon as collective curvature sensing.

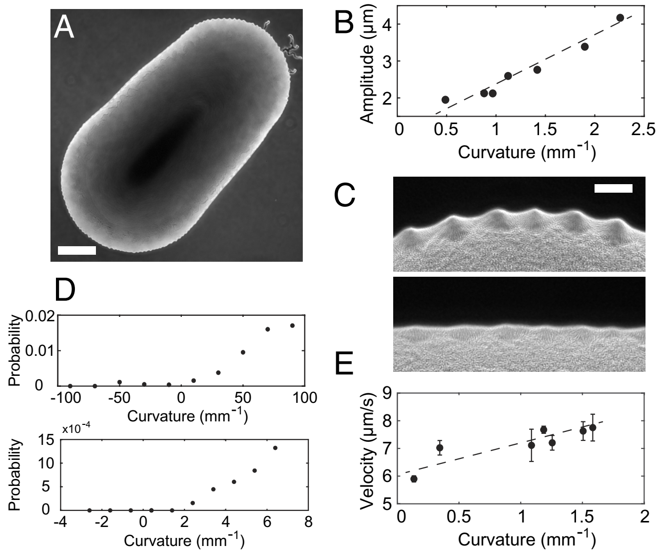

Fig. 3. Curvature dependence of protrusion amplitude and protrusion-to-branch transition probability. (*A*) Phase-contrast image of an elongated *P. mirabilis* suspension drop with creeping branches appearing only at the pole at the upper right corner, where the baseline curvature is relatively high. (Scale bar, 500 μm.) (*B*) Amplitude of interfacial protrusions plotted against the baseline curvature of the active suspension drop (*Methods*). (*C*) Enlarged view of the pole (*Upper*) and the lateral side (*Lower*) regions in panel *A*. (Scale bar 50 μm.) (*D*) Probability of a protrusion-to-branch transition at the interface of active suspension drops (*Lower*) or creeping branches (*Upper*) plotted against baseline curvature (*Methods*). Note that the curvature magnitude of creeping branches can be much larger (up to ~100 mm^{-1}) than that of the main suspension drops (up to ~8 mm^{-1}). (*E*) Collective speed of cells behind the interface of active suspension drops (ranging from ~20 to ~50 μm from the boundary) plotted against baseline curvature.

The light-induced motility deactivation experiment described above (*SI Appendix*, Fig. S1) suggests that the protrusion amplitude is related to the magnitude of active stress generated by cells. Therefore, the collective curvature sensing may result from active stress heterogeneity in the active suspension drop. To examine this idea, we measured the collective cellular speed behind the boundary (ranging from ~20 to ~50 μm from the interface) at different locations within anisotropic active drops; collective speed increases with active force in quasi-2D active bacterial suspensions in contact with a frictional substrate. Indeed, we found that the bacteria had a higher collective speed behind the boundary regions with greater curvature, while the cell density was almost homogeneous (Fig. 3*E* and *SI Appendix*, Fig. S6). The curvature-dependence of the active-stress distribution also explains the differential probability of protrusion-to-branch transitions: At boundary regions with a higher baseline curvature, the higher collective active stress can more easily overcome the liquid–air interfacial tension, thus giving rise to higher probabilities of branch invasion.

Numerical Simulations Explain the Interface Morphology and Collective Curvature Sensing. Our experiments suggest that the interfacial patterning is likely driven by active stresses produced by motile bacteria in the suspension drop. To examine this idea, we ran continuum simulations describing the suspension droplet as a 2D active nematic fluid and measuring the collective velocity and nematic order parameter (*Methods*). Guided by the experiments, the strength of nematic order was taken to decay from the edge to the center. As initial conditions we took the director field parallel to the interface with an imposed noise and zero velocity field, mimicking the parallel anchoring of cells at the interface in experiments. Extensile active fluids are unstable, and at early times, a bend instability formed around the drop, thus initiating protrusions at approximately regular positions around the interface (Fig. 4 *A* and *B*, *Top*). The director configuration within the protrusions led to outward radial flow which in turn increased the definition of the protrusions and resulted in a director field resembling a +1/2 topological defect within each protrusion, as observed in the experiments (compare Fig. 4 *B*, *Top* and Fig. 1 *B*, *Middle*). Note also the alternating planar (between the protrusions) and perpendicular (under the protrusions) director field at the edge of the main drop. We then mimicked the very low velocity of the bacteria within the protrusions by reducing the activity to zero within the protrusions. The alternating director field at the drop edge acted as boundary conditions to stabilize a flow-vortex lattice with the same structure as in the experiments (compare Fig. 4 *B*, *Bottom* and Fig. 1 *B*, *Bottom*). This was a persistent state until we reintroduced a small activity within the protrusions. They then slowly grew and eventually active material escaped from certain of the protrusions, as the creeping branches did in the experiments.

The agreement between the phenomena in experiments and continuum modeling supports the notion that the bacterial suspension drop can be described as an active drop whose dynamics is driven by cell motility. Our simulations suggest that the regularity of protrusion distribution along the interface is rooted in the bend instability. Indeed, the simulations showed that the distance between the protrusions (or protrusion width, which is roughly half of the protrusion separation) does not depend on system size or geometry but is set by the active length scale $\sim c_0\sqrt{K_Q/\zeta}$, (with some arbitrary coefficient at the front), where K_Q is the Frank elastic constant, ζ is an activity constant, and c_0 is a dimensionless coefficient (Fig. 4*C*; *Methods*). The coefficient c_0 can be found by measuring the average distance between defects in large-scale simulations in bulk. To explain collective curvature sensing as found in the experiment, we ran simulations of an elliptical active drop. In agreement with the experiment, the result shows that the protrusions first start growing in the regions of higher curvature (Fig. 4*D*), with the velocity near the interface of the elliptical drop proportional to curvature (Fig. 4*E*). This result can be understood as follows in the framework of our continuum model. The active force is proportional to the divergence of the Q-tensor and is increased by the bend distortion imposed on the director field by a curved interface. This is due to the parallel alignment of the director with the interface, promoted by both the anchoring term in the free energy and the extensile stress (48). Since the director is aligned with a curved surface, it deviated from the nematic alignment and forms a bend that produces flows. Moreover, we looked at the dynamics of the interface at large times and found that, similarly to the experiment, when branches become elongated enough, they undergo another bend instability and form new branches (Fig. 4 *F* and *G* and Movie S6). Although numerical resolution and lack of cell growth in the model prevent us from reproducing the large number of consecutive protrusion-to-branch transitions observed experimentally, this result provides additional evidence that the fractal-like pattern is created by consecutive bend instabilities due to active flows.

Discussion

Taken together, we have identified a unique mode of active matter invasion mediated by the interaction between activity-induced flows and deformable interfaces. In this mode, active drops of bacterial suspensions develop regularly spaced interfacial protrusions at the edge; the protrusions further transform into creeping branches in a hierarchical, self-similar manner, with the transition

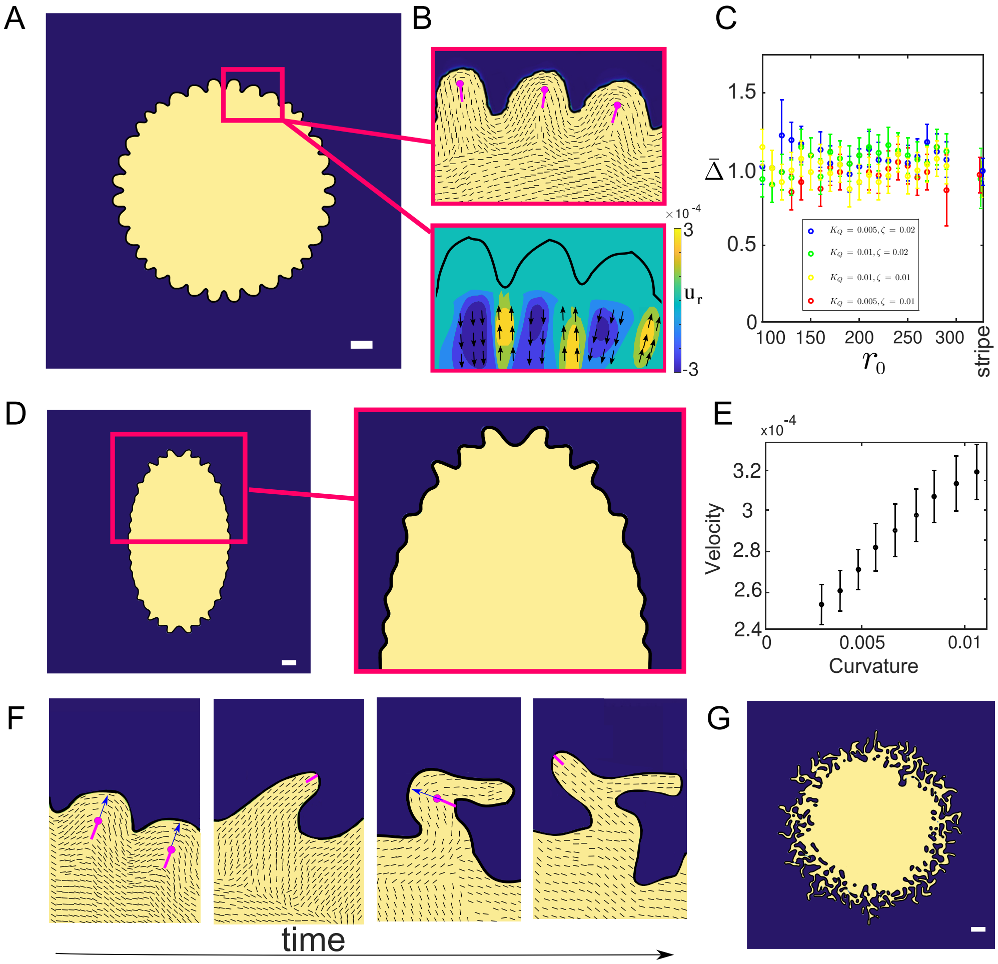

Fig. 4. Deformation of an active droplet due to extensile active stress. All the scale bars are 15 lattice Boltzmann units. (*A*) A periodic pattern of protrusions forms at the interface of the droplet. (*B*) Enlarged view of the pink box in panel *A*. *Top*: Orientation field around the protrusions. Magenta marks represent +1/2 defects. *Bottom*: Color map showing the averaged radial velocity field. Arrows indicate velocity direction. A positive value indicates moving outward toward the interface, while a negative value indicates moving inward away from the interface. (*C*) The distance between adjacent protrusions $\bar{\Delta}$ (rescaled with active length-scale $c_0\sqrt{K_Q/\zeta}$) as a function of drop radius r_0. The color of data points indicates different active length scales (blue: $K_Q = 0.005, \zeta = 0.02$; green: $K_Q = 0.01, \zeta = 0.02$; yellow: $K_Q = 0.01, \zeta = 0.01$; red: $K_Q = 0.005, \zeta = 0.01$). The collapse of data in different colors shows that $\bar{\Delta}$ is set by the active length scale. The data of $\bar{\Delta}$ in simulations with a stripe-shaped geometry with width equal to 20 lattice Boltzmann units also collapse to a similar value when rescaled with $c_0\sqrt{K_Q/\zeta}$ (right-most part of the plot), showing that the average distance between protrusions in creeping branches is also set by the active length scale. (*D*) Formation of protrusions in an elliptical droplet. The protrusions first start growing in regions with higher curvature (poles). (*E*) Average velocity at the interface of the elliptical droplet as a function of the curvature, before the formation of defects. (*F*) As time passes, +1/2 defects move and form branches (elongated arms with nematic order). The elongated arms can then undergo a bend instability and form another arm. (*G*) At very large times, all the arms have undergone bend instabilities, forming a pattern with many branches.

probability depending on the local interface curvature. Continuum simulations of an active drop model reveal that the highly ordered pattern of interfacial protrusion is initiated by bend instabilities and that enhanced active forces near high-curvature regions result in curvature-dependent protrusion dynamics which we term collective curvature sensing.

Self-organized pattern formation is a hallmark of living systems and a promising route to engineer functionalities of living materials (49). Ranging from bacterial colony development (42, 50) to animal embryogenesis (51), the formation of biological spatial patterns generally requires a complex interplay of genetic regulation, intercellular communication, and mechanical feedback (52–54). By contrast, the ordered protrusion and branching pattern reported here relies on purely physical interactions between activity-induced flows and deformable interfaces. In particular, the phenomenon of collective curvature sensing shows that interface geometry may play important roles in active matter morphogenesis. It suggests a strategy, i.e., designing curvature cues at the interface of active fluids, to guide and manipulate pattern formation in active materials.

While we expect that the mode of ordered invasion and pattern formation applies to nematic active fluids in general, our findings are of direct relevance to the expansion and dispersal of bacterial communities. Bacterial communities in ecological and clinical settings are commonly found in interface-associated environments, such as biofilms (55, 56) and bacterial swarms (18, 57) that develop on solid substrates. If the substrates are highly wettable, communities of motile bacteria can establish a thin liquid film and explore new space rapidly by a process known as swarming, in which flagellar motility drives uniform expansion of the liquid film (58, 59). However, swarming is inhibited on substrates with low wettability (e.g., high-concentration agar substrates in laboratory settings or substrates without wetting agents). Under such circumstances, the protrusion-to-branch transition becomes a viable solution for bacterial communities to explore new territories.

Methods

No statistical methods were used to predetermine sample size.

Bacterial Strains. The following two strains were used: wild-type *P. mirabilis* BB2000, and a fluorescent *P. mirabilis* KAG108 [BB2000 background with constitutive expression of Green Fluorescent Protein (GFP) and with an ampicillin resistance marker (60); from Karine Gibbs, Harvard University, Cambridge, MA]. Single-colony isolates were grown overnight (~13 to 14 h) with shaking in LB medium (1% Bacto tryptone, 0.5% yeast extract, 0.5% NaCl) at 30 °C to stationary phase. For *P. mirabilis* KAG108, ampicillin (100 μg/mL) was added to the growth medium to maintain the plasmid.

Agar Plates. LB agar (Difco Bacto agar at specified concentrations infused with 1% Bacto tryptone, 0.5% yeast extract, 0.5% NaCl) was autoclaved and stored at room temperature. Before use, the agar was melted in a microwave oven, cooled to ~60 °C, and pipetted in 10-mL aliquots into 90-mm polystyrene Petri plates. The plates were swirled gently to ensure surface flatness, cooled for 10 min without a lid inside a large Plexiglas box, and then covered by the lid for further experimentation.

Preparation of Bacterial Active Suspension Drops. Two approaches, namely colony growth and direct deposition, were adopted to prepare bacterial active suspension drops containing *P. mirabilis*. For the colony growth method, overnight *P. mirabilis* cultures were inoculated onto a 0.6% LB agar plate (as described above) by forcibly collapsing a bubble consisting of the bacterial culture, forming a lawn of circular inocula with a diameter 270 ± 120 μm (mean ± SD, N = 35). The inoculated plates were dried for 10 min without a lid inside the Plexiglas box. The plates were then covered and incubated at 30 °C and ~95% relative humidity in an incubator with a water tray; within the experimental observation time, the *P. mirabilis* inocula as prepared do not swarm under this humidity due to the lack of synthesis of wetting agents. The plates were incubated for ~20 h. The *P. mirabilis* inocula incubated for this duration of time reached a size of ~0.5 to 2 mm in diameter and a height of ~20 to 30 μm at the center, and most cells were highly motile except those near the center. After the emergence of interfacial protrusions, it took a variable time for creeping branches to emerge, ranging from a few hours to ~10 h depending on the size of the active suspension drops. Two or more circular bacterial suspension drops at close proximity could merge due to growth-induced expansion, forming an elongated or elliptical suspension drop. As the expansion speed of droplets driven by cell growth is much smaller than the speed of protrusion and branching driven by cell motility, the shape of active drops remains similar during the experiments. To prepare bacterial active suspension drops by direct deposition, we collected highly motile cells from *P. mirabilis* colonies grown on 2.0% LB agar (incubated at 30 °C and ~40% relative humidity for ~20 h), washed by centrifugation, and resuspended to a volume fraction of ~10% in fresh medium. Approximately 0.1 to 0.2 μL of the resuspended *P. mirabilis* culture was then deposited onto fresh 2.0 to 3.0% agar surface (which does not support swarming of *P. mirabilis* within the experimental observation time) to form a circular bacterial suspension drop of ~1.5 to 2 mm in diameter. After depositing the active suspension drops, interfacial protrusions appeared in ~1 to 5 min, the ordered interfacial morphological pattern as shown in Fig. 1 stabilized within ~10 min (Movie S3), and the protrusion-to-branch transition normally occurred in ~20 min. To assess bacterial number density in active suspension drops by fluorescence intensity, wild-type *P. mirabilis* was replaced with GFP-tagged *P. mirabilis* KAG108 in the above experiments.

Microscopy Imaging. All imaging was performed on a motorized inverted microscope (Nikon TI-E). The phase-contrast images of bacterial active suspension drops, interfacial protrusions, and creeping branches were acquired with 20× (Nikon S Plan Fluor 20×, numerical aperture 0.45, working distance 8.2-6.9 mm), 10× (Nikon CFI Achromat 10×, numerical aperture 0.25, working distance 7.0 mm) or 4× (Nikon Plan Fluor 4×, numerical aperture 0.13, working distance 16.5 mm) objectives; the images were recorded by a scientific complementary metal-oxide-semiconductor (sCMOS) camera (Andor Zyla 4.2 PLUS USB 3.0) at 10 fps and at full frame size (2,048×2,048 pixels). To tune the speed of cells in the bacterial suspension, cells were illuminated by violet light of ~1,740 mW/cm^2 provided by Nikon Intensilight and passing through the 20× objective via a 406-nm filter (406/15 nm; FF01-406/15-25, Semrock Inc.). To assess bacterial number density in active suspension drops, GFP-tagged *P. mirabilis* KAG108 cells were imaged in epifluorescence using the 20× objective and an FITC filter cube (excitation 482/35 nm, emission 536/40 nm, dichroic 506 nm; Semrock Inc.), with the excitation light provided by a mercury precentered fiber illuminator (Nikon Intensilight); the fluorescence images were recorded with the sCMOS camera (Andor Zyla 4.2 PLUS USB 3.0). In all experiments, the Petri dishes were covered with a lid to prevent evaporation and air convection. The sample temperature was maintained and controlled via a custom-built temperature-control system installed on the microscope stage.

Image Processing and Data Analysis. Images were processed using open-source Fiji (ImageJ) software (https://fiji.sc/) and custom-written programs in MATLAB (The MathWorks, Inc.). Prior to processing, the microscopy images were smoothed to reduce noise by convolution with a Gaussian kernel of SD ~1 μm. To acquire the bacterial orientation field, we first calculate the structure tensor defined as

$$J(x, y) = \begin{bmatrix} I_x I_x & I_x I_y \\ I_y I_x & I_y I_y \end{bmatrix},$$

where $I_x = \partial_x I$, $I_y = \partial_y I$, and $I = I(x, y)$ is the light intensity field of a phase-contrast image (61). As the intensity of the regions occupied by bacterial cells is different from the background in phase-contrast imaging, the spatial gradients of the intensity field that appear in the structure tensor contain information on the spatial distribution of cell orientations: For a given position (x, y), the orientation $\theta(x, y)$ of the eigenvector of the structure tensor $J(x, y)$ with greater eigenvalue typically corresponds to the local orientation of cells located at the position. The bacterial orientation field was obtained by coarse-graining the local orientations $\theta(x, y)$ with a grid size of 10 pixel × 10 pixel (3.25 μm × 3.25 μm); the mean orientation at a grid, denoted as $\langle\theta\rangle$, is computed as $\arg\left[\sum_k \exp(i2\theta_k)\right]$ (62), where arg(x) denotes the argument of the complex number x. To identify the nematic defects near the interface, we computed the net change of director angle along a counterclockwise loop around each grid, and grids with ~π director angle change were identified as the cores of +1/2 nematic defects (63). The direction of a +1/2 nematic defect is calculated as $\boldsymbol{n}_i = \frac{\nabla \cdot J(\boldsymbol{r}_i)}{\left|\nabla \cdot J(\boldsymbol{r}_i)\right|}$, where $\boldsymbol{r}_i$ is the location of the defect core (32).

To identify the protrusions at the interface of the active suspension drop, we first converted the phase-contrast image to a binary image to identify the interface. For circular active suspension drops, the active fluid interface was represented as $\rho = f(\phi)$ in a polar coordinate with the origin set as the center of the active suspension drop. For active suspension drops with an anisotropic shape, the interface was divided into ~200-μm segments; each segment was represented as $\rho = f(\phi)$ in a local polar coordinate system whose origin was chosen as the center of curvature of a circular arc that best fitted the interface segment. Next, the active fluid interface (or interface segment) was smoothed along ϕ to reduce noise by convoluting $f(\phi)$ with a Gaussian kernel of SD of $\Delta\phi = 1$ μm/$\overline{\rho}$. The protrusion peaks and valleys were identified as $\partial_\phi \rho = 0$ and $\partial_\phi^2 \rho < 0$ (for protrusion peaks) or $\partial_\phi^2 \rho > 0$ (for valleys). The amplitude of the interfacial protrusions was defined as half of the difference in averaged polar radius between protrusion peaks and valleys, i.e., $(\overline{\rho}_{peak-}\overline{\rho}_{valley})/2$. If the amplitude of a protrusion exceeds 100 μm, the protrusion is considered as having transitioned to a creeping branch.

To compute the collective velocity near the interface, we first performed optical flow analysis based on phase-contrast time-lapse videos using the built-in OpticalFlowHS function (64) of MATLAB with a grid size of 1 pixel × 1 pixel. Prior to the optical flow analysis, the microscopy images were smoothed to reduce noise by convolution with a Gaussian kernel of SD of 1 μm. The results were insensitive to different parameters of smoothing. The optical flow analysis yielded a space- and time-dependent collective velocity field $\vec{v}\,(\vec{r}, t)$, which was then decomposed in polar coordinates as $(v_r(\vec{r}, t), v_\phi(\vec{r}, t))$ (v_r denotes radial component and v_ϕ denotes tangential or azimuthal component; the origin of the polar coordinate system is chosen at the center of the circular bacterial active suspension drop). The spatial-temporal correlation of radial velocity near the interface is computed as $C(\Delta\phi, \Delta t) = \frac{\langle v_r(R, \phi, t) v_r(R, \phi + \Delta\phi, t + \Delta t)\rangle_{\phi,t}}{\langle v_r(R, \phi, t)^2\rangle_{\phi,t}}$, where $\Delta\phi$ is the polar angle difference from an arbitrary reference position on the interface, Δt is the time difference from an arbitrary instant ($\Delta t > 0$, corresponding to time lag in the correlation calculation), angular brackets $\langle \ldots \rangle_{\phi,t}$ indicate averaging over the azimuthal angle and time t, and R is the averaged radius of the active suspension drop.

To calculate the baseline curvature of the interface of active suspension drops or creeping branches, segments of the interface with a length specified below were fitted to circular arcs via the least squares method in MATLAB. The protocols for obtaining the interface segments on active suspension drops and on branches were different because the contribution from protrusions was excluded in different ways under the two circumstances: 1) To calculate the baseline curvature of active suspension drops, we first binarized a phase-contrast image (e.g., main text Fig. 3*A*) into a black-and-white (BW) image with an appropriate threshold. The BW image was convolved by a 2D Gaussian filter (SD 30 μm) to smooth out the interface protrusions. The smoothed grayscale image allowed us to extract the information of the suspension drop's interface by thresholding. The interface was then divided into segments of length ~300 μm, and local baseline curvatures were calculated based on these segments. 2) To calculate the baseline curvature of the interface of creeping branches, we had to use a different approach to exclude the contribution from protrusions because the curvature of protrusions is of a similar magnitude as that of the branches. We first binarized the original phase-contrast images of branches into black-and-white images and extracted the branch interface from the binarized images. In parallel, we computed the orientation field of cells based on the phase-contrast images, and interface protrusions were identified by the presence of $+1/2$ nematic defects in the orientation fields. Then, the branch interface associated with the identified protrusions was removed, and the remaining portion of the interface was divided into segments of length ~100 μm for the calculation of local baseline curvature.

To calculate the probabilities of protrusion-to-branch transition (Fig. 3*D*), samples of creeping branches and of main suspension drops (either with or without diverging protrusions) were processed using the protocols described above to yield interface segments for local baseline curvature calculation; the total number of these segments is ~55,000 for the active suspension drops and ~30,000 for creeping branches, respectively. Each segment was fitted to an arc to calculate the baseline curvature. According to the baseline curvature, the segments were divided into 10 groups falling into bins of the baseline curvature ranging from -100 to 100 mm^{-1} (for data of creeping branches) or from -3.3 to 7.3 mm^{-1} (for data of suspension drops). For the average baseline curvature corresponding to each group, we calculate the probability of protrusion-to-branch transition as the ratio between the number of diverging and nondiverging segments within the group.

Continuum Simulation of the 2D Active Nematic Fluid Drop Model. We use the active nematohydrodynamic equations, the fundamental continuum equations that describe wet active nematic (65–68). These are coupled equations for the evolution of the bacteria concentration field ϕ, nematic tensor, $\mathbf{Q} = S(\mathbf{nn} - \mathbf{I}/2)$ in two dimensions, and the associated incompressible fluid velocity, $\mathbf{u}$. They read

$$\partial_t \mathbf{Q} + \mathbf{u} \cdot \nabla \mathbf{Q} - \mathcal{W} = \gamma \mathbf{H}, \qquad [\mathbf{1}]$$

$$\rho\left(\partial_t + \mathbf{u} \cdot \nabla\right)\mathbf{u} = \nabla \cdot \boldsymbol{\Pi} - \Gamma_f\ \mathbf{u}, \quad \nabla \cdot \mathbf{u} = 0 \qquad [\mathbf{2}]$$

$$\partial_t \phi + \mathbf{u} \cdot \nabla \phi = \Gamma_\phi \nabla^2 \mu, \qquad [\mathbf{3}]$$

$$\mu = \frac{\partial f}{\partial \phi} - \nabla \cdot \left(\frac{\partial f}{\partial \nabla \phi}\right), \qquad [\mathbf{4}]$$

$$\begin{aligned} f = {} & \frac{C}{2}\left(\mathcal{J}\phi - \frac{Q_{ij}Q_{ij}}{2}\right)^2 + \frac{A}{2}\phi^2(1-\phi)^2 + \frac{K_\phi}{2}\nabla_m \phi \nabla_m \phi \\ & + \frac{K_Q}{2}\nabla_m Q_{ij} \nabla_m Q_{ij} + a \nabla_i \phi Q_{ij} \nabla_j \phi. \end{aligned} \qquad [\mathbf{5}]$$

In the definition of the nematic tensor, the director field $\mathbf{n}$ represents the orientation of the nematic alignment, and the magnitude of the nematic order is denoted by S. In the evolution of the $\mathbf{Q}$ tensor, γ is the rotational diffusivity, and the molecular field, $\boldsymbol{H} = -\partial f / \partial \boldsymbol{Q} + \nabla \cdot \left(\partial f / \partial \nabla \mathbf{Q}\right)$, drives the nematic tensor toward the minimum of the free energy (**5**). The generalized advection term

$$\mathcal{W} = (\lambda \mathbf{E} + \boldsymbol{\Omega}) \cdot \left(\mathbf{Q} + \frac{\mathbf{I}}{2}\right) + \left(\mathbf{Q} + \frac{\mathbf{I}}{2}\right) \cdot (\lambda \mathbf{E} - \boldsymbol{\Omega}) - \lambda(\mathbf{Q} + \mathbf{I})Tr(\mathbf{Q} \cdot \mathbf{E}), \qquad [\mathbf{6}]$$

models the response of the nematic field to the strain rate $\mathbf{E}$ and vorticity $\boldsymbol{\Omega}$, and λ denotes the flow-aligning parameter. In the Navier–Stokes equation (**2**), ρ is the density of the suspension, Γ_f is a friction coefficient, and the stress tensor, $\boldsymbol{\Pi}$, includes viscous, elastic, and active contributions. The viscous stress, $\boldsymbol{\Pi}^v = 2\eta \mathbf{E}$, where η is the viscosity, and the elastic stress,

$$\begin{aligned} \Pi_{ij}^p = {} & -P\delta_{ij} + \lambda\left(Q_{ij} + \delta_{ij}\right)Q_{kl}H_{kl} - \lambda H_{ik}\left(Q_{kj} + \frac{\delta_{kj}}{2}\right) \\ & - \lambda\left(Q_{ik} + \frac{\delta_{ik}}{2}\right)H_{kj} + Q_{ik}H_{kj} - H_{ik}Q_{kj} - K\left(\partial_i Q_{kl}\right)\left(\partial_j Q_{kl}\right), \end{aligned} \qquad [\mathbf{7}]$$

where P is the pressure. These are familiar terms that appear in the dynamical equations of passive liquid crystals. Activity enters through an active stress $\boldsymbol{\Pi}^a = -\zeta \mathbf{Q}$, where, for the extensile systems studied in this paper, $\zeta > 0$. Eq. **3** describes the evolution of the concentration of bacteria, where Γ_ϕ shows how fast ϕ responds to gradients in the chemical potential μ. The first term in the free-energy density equation (Eq. **5**) stabilizes a nematic phase inside the drop (where $\phi \neq 0$). The second and third terms in Eq. **5** stabilize the circular droplet; they are Cahn–Hilliard-type free energies describing soft boundaries with the length of the transition regions between bacteria and the surrounding fluid proportional to $\sqrt{K_\phi / A}$, where K_ϕ is the surface tension coefficient and A is the coefficient associated with phase separation of two fluids. The fourth term in Eq. **5** is the energy cost due to distortions in the nematic field, assuming a single Frank elastic constant K_Q. Finally, the last term in Eq. **5** is an anchoring free energy which favors parallel anchoring of the director at the interface for $a < 0$.

In the experiments, the nematic alignment of the bacteria decreases toward the center of the drop. To mirror this in the simulations, the magnitude of the nematic order inside the drop is set by a field $\mathcal{J}$ with dynamics

$$\partial_t \mathcal{J} = D_s \nabla^2 \mathcal{J} - k_s \phi, \qquad [\mathbf{8}]$$

and with the boundary condition that $\mathcal{J} = 1$outside the drop and also at the interface if $\phi < 0.5$. This dynamic results in the magnitude of the order, and as a result the magnitude of the active stress, decaying toward the center of the drop. Inside the drop, the magnitude of the nematic order is related to the field $\mathcal{J}$ through the relation $S^2 = \mathcal{J}$, and outside, the drop S is equal to zero. Eq. **8** allows for the formation of periodic patterns at the interface. Studies of active droplets in which the nematic order is constant throughout the droplet have shown formation of protrusions at the interface, but these are due to defects formed in the center of the droplet, and the resulting patterns are not periodic (69). In our simulations and experiments, the deformations are caused by defects and distortions of the nematic field that form near the interface.

The deformation of the boundary in our model is mainly caused by the velocity of the active nematic material (through a term $\mathbf{u} \cdot \nabla \phi$ in Eq. **3**). We note that Laplacian growth models produce fingering at the interface between two immiscible passive fluids (70). Laplacian growth models describe the patterns that form at the interface between two fluids with different viscosities, by assuming that the velocity of the fluid is proportional to the gradient in pressure. In our model, the velocity is a function of cell orientation, and the interface dynamics is affected by flows created by the bacteria. The elasticity and the active flows both enter the dynamics of the nematic tensor and lead to formation of defects. The defects themselves create more flows, and so the dynamics of boundary deformation in our model is different from Laplacian growth.

The equations of active nematohydrodynamics are solved using a hybrid lattice Boltzmann and finite difference method in a square box with periodic boundary conditions (65, 71). For the simulations of the circular drop in Fig. 4 *A*–*C*, *F*, and *G* and Movie S6 in *SI Appendix*, we used the parameter values: $D_s = 0.1$, $\rho = 40$, $\gamma = 0.3$, $k_s = 0.0002$, ζ from 0.01 to 0.02, $\Gamma_f = 0.3$, K_Q from 0.005 to 0.01, $K_\phi = 0.01$, $C = 0.001$, $A = 0.1$, $\Gamma_\phi = 0.1$, $\lambda = 0$, $a = -0.005$. The size of the simulation box and the total time of the simulation were $L = 450$ and $t_{tot} = 5 \times 10^5$in lattice Boltzmann units, and the radius of the drop was $r_0 = 150$. The simulations were initialized with the director parallel to the interface and with a uniform noise in the interval $[0, 3\pi] \times 10^{-2}$. To calculate the director and the average velocity field in Fig. 4*B*, we fixed the edge of the drop once the protrusions and the defects had formed and averaged the flow in the vicinity of sufficiently wide protrusions.

For the ellipse in Fig. 4 *D* and *E*, we chose the long and short axis equal to $r_2 = 150$ and $r_1 = 85$, respectively. We added an initial noise uniformly distributed in the interval $[0, \pi] \times 10^{-3}$. All the other parameters were the same as above. In Fig. 4*E*, we averaged the velocity field at the scale of each protrusion when small protrusions form. The curvature is the curvature of the original ellipse.

Data, Materials, and Software Availability. All study data are included in the article and/or supporting information. The data can also be accessed at: doi: 10.57760/sciencedb.09346 (72).

ACKNOWLEDGMENTS. We thank Karine Gibbs (Harvard University) for providing the bacterial strains. This work was supported by the Ministry of Science and Technology Most China (MOST No. 2020YFA0910700, to Y.W.), the Research Grants Council of Hong Kong SAR (RGC Ref. No. 14307821, 14306820, RFS2021-4S04; to Y.W.), and National Natural Science Foundation of China (NSFC No. 31971182, to Y.W.). M.R.N. acknowledges the support of the Clarendon Fund Scholarships.

1. M. C. Marchetti *et al.*, Hydrodynamics of soft active matter. *Rev. Modern Phys.* **85**, 1143–1189 (2013).
2. D. Saintillan, Rheology of active fluids. *Annu. Rev. Fluid Mech.* **50**, 563–592 (2018).
3. H. H. Wensink *et al.*, Meso-scale turbulence in living fluids. *Proc. Natl. Acad. Sci. U.S.A.* **109**, 14308–14313 (2012).
4. H. M. López, J. Gachelin, C. Douarche, H. Auradou, E. Clément, Turning bacteria suspensions into superfluids. *Phys. Rev. Lett.* **115**, 028301 (2015).
5. S. Liu, S. Shankar, M. C. Marchetti, Y. Wu, Viscoelastic control of spatiotemporal order in bacterial active matter. *Nature* **590**, 80–84 (2021).
6. T. B. Saw *et al.*, Topological defects in epithelia govern cell death and extrusion. *Nature* **544**, 212 (2017).
7. R. Alert, X. Trepat, Physical models of collective cell migration. *Annu. Rev. Condens. Matter Phys.* **11**, 77–101 (2020).
8. F. C. Keber *et al.*, Topology and dynamics of active nematic vesicles. *Science* **345**, 1135–1139 (2014).
9. K.-T. Wu *et al.*, Transition from turbulent to coherent flows in confined three-dimensional active fluids. *Science* **355**, eaal1979 (2017).
10. P. Galajda, J. Keymer, P. Chaikin, R. Austin, A wall of funnels concentrates swimming bacteria. *J. Bacteriol.* **189**, 8704–8707 (2007).
11. G. Lambert, D. Liao, R. H. Austin, Collective escape of chemotactic swimmers through microscopic ratchets. *Phys. Rev. Lett.* **104**, 168102 (2010).
12. H. Wioland, E. Lushi, R. E. Goldstein, Directed collective motion of bacteria under channel confinement. *New J. Phys.* **18**, 075002 (2016).
13. H. Wioland, F. G. Woodhouse, J. Dunkel, J. O. Kessler, R. E. Goldstein, Confinement stabilizes a bacterial suspension into a spiral vortex. *Phys. Rev. Lett.* **110**, 268102 (2013).
14. H. Xu, J. Dauparas, D. Das, E. Lauga, Y. Wu, Self-organization of swimmers drives long-range fluid transport in bacterial colonies. *Nat. Commun.* **10**, 1792 (2019).
15. D. Nishiguchi, I. S. Aranson, A. Snezhko, A. Sokolov, Engineering bacterial vortex lattice via direct laser lithography. *Nat. Commun.* **9**, 4486 (2018).
16. A. G. Clark, D. M. Vignjevic, Modes of cancer cell invasion and the role of the microenvironment. *Curr. Opin. Cell Biol.* **36**, 13–22 (2015).
17. X. Li, A. Das, D. Bi, Mechanical heterogeneity in tissues promotes rigidity and controls cellular invasion. *Phys. Rev. Lett.* **123**, 058101 (2019).
18. D. B. Kearns, A field guide to bacterial swarming motility. *Nat. Rev. Microbiol.* **8**, 634–644 (2010).
19. A. Persat *et al.*, The mechanical world of bacteria. *Cell* **161**, 988–997 (2015).
20. C. J. Miles, A. A. Evans, M. J. Shelley, S. E. Spagnolie, Active matter invasion of a viscous fluid: Unstable sheets and a no-flow theorem. *Phys. Rev. Lett.* **122**, 098002 (2019).
21. F. Kempf, R. Mueller, E. Frey, J. M. Yeomans, A. Doostmohammadi, Active matter invasion. *Soft Matter* **15**, 7538–7546 (2019).
22. L. Le Nagard *et al.*, Encapsulated bacteria deform lipid vesicles into flagellated swimmers. *Proc. Natl. Acad. Sci. U.S.A.* **119**, e2206096119 (2022).
23. G. Kokot, H. A. Faizi, G. E. Pradillo, A. Snezhko, P. M. Vlahovska, Spontaneous self-propulsion and nonequilibrium shape fluctuations of a droplet enclosing active particles. *Commun. Phys.* **5**, 91 (2022).
24. M. Spellings *et al.*, Shape control and compartmentalization in active colloidal cells. *Proc. Natl. Acad. Sci. U.S.A.* **112**, E4642–E4650 (2015).
25. M. Paoluzzi, R. Di Leonardo, M. C. Marchetti, L. Angelani, Shape and displacement fluctuations in soft vesicles filled by active particles. *Sci. Rep.* **6**, 34146 (2016).
26. S. C. Takatori, A. Sahu, Active contact forces drive nonequilibrium fluctuations in membrane vesicles. *Phys. Rev. Lett.* **124**, 158102 (2020).
27. H. R. Vutukuri *et al.*, Active particles induce large shape deformations in giant lipid vesicles. *Nature* **586**, 52–56 (2020).
28. L. J. Ruske, J. M. Yeomans, Morphology of active deformable 3D droplets. *Phys. Rev. X* **11**, 021001 (2021).
29. R. Alert, Fingering instability of active nematic droplets. *J. Phys. A Math. Theor.* **55**, 234009 (2022).
30. G. Hauser, *Über Fäulnisbakterien und deren Beziehung zur Septicämie* (F.G.W. Vogel, Leipzig, Germany, 1885).
31. O. Rauprich *et al.*, Periodic phenomena in *Proteus mirabilis* swarm colony development. *J. Bacteriol.* **178**, 6525–6538 (1996).
32. A. J. Vromans, L. Giomi, Orientational properties of nematic disclinations. *Soft Matter* **12**, 6490–6495 (2016).
33. M. Basan, J.-F. Joanny, J. Prost, T. Risler, Undulation instability of epithelial tissues. *Phys. Rev. Lett.* **106**, 158101 (2011).
34. S. M. Troian, X. L. Wu, S. A. Safran, Fingering instability in thin wetting films. *Phys. Rev. Lett.* **62**, 1496–1499 (1989).
35. H. Du *et al.*, High density waves of the bacterium pseudomonas aeruginosa in propagating swarms result in efficient colonization of surfaces. *Biophys. J.* **103**, 601–609 (2012).
36. M. Fauvart *et al.*, Surface tension gradient control of bacterial swarming in colonies of *Pseudomonas aeruginosa*. *Soft Matter* **8**, 70–76 (2012).
37. S. Trinschek, K. John, U. Thiele, Modelling of surfactant-driven front instabilities in spreading bacterial colonies. *Soft Matter* **14**, 4464–4476 (2018).
38. C. Giverso, M. Verani, P. Ciarletta, Branching instability in expanding bacterial colonies. *J. R. Soc. Interface* **12**, 20141290 (2015).
39. R. Daniels, J. Vanderleyden, J. Michiels, Quorum sensing and swarming migration in bacteria. *FEMS Microbiol. Rev.* **28**, 261–289 (2004).
40. L. S. Liebovitch, T. Toth, A fast algorithm to determine fractal dimensions by box counting. *Phys. Lett. A* **141**, 386–390 (1989).
41. T. Matsuyama, M. Matsushita, Fractal morphogenesis by a bacterial cell population. *Critical Rev. Microbiol.* **19**, 117–135 (1993).
42. E. Ben-Jacob, From snowflake formation to growth of bacterial colonies II: Cooperative formation of complex colonial patterns. *Contemp. Phys.* **38**, 205–241 (1997).
43. D. A. Kessler, H. Levine, Pattern formation in Dictyostelium via the dynamics of cooperative biological entities. *Phys. Rev. E* **48**, 4801 (1993).
44. P. J. Plath, "Fractal aggregation of *Dictyostelium discoideum*" in *Imagery Synergetics: Science of Cooperation* (Springer International Publishing, Cham, 2022), pp. 371–377.
45. A. Takamatsu, T. Gomi, T. Endo, T. Hirai, T. Sasaki, Energy-saving with low dimensional network in Physarum plasmodium. *J. Phys. D: Appl. Phys.* **50**, 154003 (2017).
46. M. Kramar, K. Alim, Encoding memory in tube diameter hierarchy of living flow network. *Proc. Natl. Acad. Sci. U.S.A.* **118**, e2007815118 (2021).
47. L. Pieuchot *et al.*, Curvotaxis directs cell migration through cell-scale curvature landscapes. *Nat. Commun.* **9**, 3995 (2018).
48. M. L. Blow, S. P. Thampi, J. M. Yeomans, Biphasic, lyotropic, active nematics. *Phys. Rev. Lett.* **113**, 248303 (2014).
49. A. Y. Chen, C. Zhong, T. K. Lu, Engineering living functional materials. *ACS Synth. Biol.* **4**, 8–11 (2015).
50. E. O. Budrene, H. C. Berg, Dynamics of formation of symmetrical patterns by chemotactic bacteria. *Nature* **376**, 49–53 (1995).
51. D. A. Melton, Pattern formation during animal development. *Science* **252**, 234–241 (1991).
52. J. D. Murray, P. K. Maini, R. T. Tranquillo, Mechanochemical models for generating biological pattern and form in development. *Phys. Rep.* **171**, 59–84 (1988).
53. A. Koch, H. Meinhardt, Biological pattern formation: From basic mechanisms to complex structures. *Rev. Modern Phys.* **66**, 1481 (1994).
54. N. Luo, S. Wang, L. You, Synthetic pattern formation. *Biochemistry* **58**, 1478–1483 (2019).
55. L. Hall-Stoodley, J. W. Costerton, P. Stoodley, Bacterial biofilms: From the natural environment to infectious diseases. *Nat. Rev. Microbiol.* **2**, 95–108 (2004).
56. D. López, H. Vlamakis, R. Kolter, Biofilms. *Cold Spring Harb. Perspect. Biol.* **2**, a000398 (2010).
57. R. M. Harshey, Bacterial motility on a surface: Many ways to a common goal. *Annu. Rev. Microbiol.* **57**, 249–273 (2003).
58. R. Zhang, L. Turner, H. C. Berg, The upper surface of an *Escherichia coli* swarm is stationary. *Proc. Natl. Acad. Sci. U.S.A.* **107**, 288–290 (2010).
59. Y. Wu, H. C. Berg, Water reservoir maintained by cell growth fuels the spreading of a bacterial swarm. *Proc. Natl. Acad. Sci. U.S.A.* **109**, 4128–4133 (2012).
60. K. A. Gibbs, M. L. Urbanowski, E. P. Greenberg, Genetic determinants of self identity and social recognition in bacteria. *Science* **321**, 256–259 (2008).
61. A. M. Bazen, S. H. Gerez, Systematic methods for the computation of the directional fields and singular points of fingerprints. *IEEE Trans. Pattern Anal. Mach. Intell.* **24**, 905–919 (2002).
62. F. Peruani, F. Ginelli, M. Bär, H. Chaté, Polar vs. apolar alignment in systems of polar self-propelled particles. *J. Phys. Conf. Ser.* **297**, 012014 (2011).
63. T. C. Lubensky, D. Pettey, N. Currier, H. Stark, Topological defects and interactions in nematic emulsions. *Phys. Rev. E* **57**, 610–625 (1998).
64. B. K. P. Horn, B. G. Schunck, Determining optical flow. *Artif. Intell.* **17**, 185–203 (1981).
65. D. Marenduzzo, E. Orlandini, M. E. Cates, J. M. Yeomans, Steady-state hydrodynamic instabilities of active liquid crystals: Hybrid lattice Boltzmann simulations. *Phys. Rev. E* **76**, 031921 (2007).
66. M. E. Cates, O. Henrich, D. Marenduzzo, K. Stratford, Lattice Boltzmann simulations of liquid crystalline fluids: Active gels and blue phases. *Soft Matter* **5**, 3791–3800 (2009).
67. L. N. Carenza, G. Gonnella, A. Lamura, G. Negro, A. Tiribocchi, Lattice Boltzmann methods and active fluids. *Eur. Phys. J. E* **42**, 1–38 (2019).
68. J. Hardoüin *et al.*, Reconfigurable flows and defect landscape of confined active nematics. *Commun. Phys.* **2**, 121 (2019).
69. A. Doostmohammadi, S. P. Thampi, J. M. Yeomans, Defect-mediated morphologies in growing cell colonies. *Phys. Rev. Lett.* **117**, 048102 (2016).
70. M. Z. Bazant, D. Crowdy, "Conformal mapping methods for interfacial dynamics" in *Handbook of Materials Modeling: Methods*, S. Yip, Ed. (Springer, Netherlands, Dordrecht, 2005), pp. 1417–1451.
71. F. Mackay, J. Toner, A. Morozov, D. Marenduzzo, Darcy's law without friction in active nematic rheology. *Phys. Rev. Lett.* **124**, 187801 (2020).
72. Y. Wu, Data from: Geometrical control of interface patterning underlies active matter invasion. SCIENCE DATA BANK. https://doi.org/10.57760/sciencedb.09346. Deposited 3 July 2023.